

# A graph generation pipeline for critical infrastructures based on heuristics, images and depth data

Mike Diessner<sup>1,\*</sup> and Yannick Tarant<sup>1</sup>

<sup>1</sup>German Aerospace Center, Institute for the Protection of Terrestrial Infrastructures, Sankt Augustin, Germany

Correspondence\*:

Mike Diessner, German Aerospace Center, Institute for the Protection of Terrestrial Infrastructures, Rathausallee 12, 53757 Sankt Augustin, Germany  
mike.diessner@dlr.de

## 2 ABSTRACT

3 Virtual representations of physical critical infrastructures, such as water or energy plants, are  
4 used for simulations and digital twins to ensure resilience and continuity of their services. These  
5 models usually require 3D point clouds from laser scanners that are expensive to acquire and  
6 require specialist knowledge to use. In this article, we present a prototypical graph generation  
7 pipeline based on photogrammetry. The pipeline detects relevant objects and predicts their  
8 relation using RGB images and depth data generated by a stereo camera. This more cost-  
9 effective approach uses deep learning for object detection and instance segmentation of the  
10 objects, and employs user-defined heuristics or rules to infer their relations. Results of two  
11 hydraulic systems show that this strategy can produce graphs close to the ground truth. While  
12 this study focuses on hydraulic systems, the general process can be used to tailor the method  
13 to other types of infrastructures and applications. The user-defined rules create transparency  
14 qualifying the pipeline to be used in the high stakes decision-making that is required for critical  
15 infrastructures.

16 **Keywords:** Graph generation, relational graph, critical infrastructure, photogrammetry, depth data, image data, scene understanding,  
17 digital twin

## 1 INTRODUCTION

18 Critical infrastructures are assets, organizations or facilities that are integral to the survival and functioning  
19 of a nation and its society. Disturbances in their services can have major adverse impacts, such as supply  
20 shortages, increased risks to public health and national security, or disruptions of financial services and the  
21 broader economy. Critical infrastructures can be physical or virtual assets and appear in sectors such as  
22 energy, healthcare, food, water, transportation, communication, nuclear systems and more (Osei-Kyei et al.,  
23 2021; Alcaraz and Zeadally, 2015; Yusta et al., 2011).

24 Methods such as simulations and digital twins are used to monitor, maintain and optimize infrastructures,  
25 and to prepare and train for worst-case scenarios by simulating extreme and often rare events. Thus, these  
26 methods have the potential to increase resilience, security, performance and continuity of infrastructures  
27 and are an invaluable tool to ensure national security and well-being (Lampropoulos et al., 2024; Sousa

et al., 2021). In many cases, a digital twin of a physical asset, such as a nuclear facility or a water treatment plant, requires a virtual copy of the objects (e.g., pipes, pumps and valves) and their relation to each other to be used for simulations or training in virtual reality. The process of generating these models requires a large amount of manual work and is thus expensive and time-consuming (Franke et al., 2023). Most existing methods use laser scanners to gather 3D point clouds of the facilities that are then processed and analyzed. However, these scanners are expensive, creating demand for methods using more affordable and accessible equipment, such as stereo cameras.

The main objective of this article is the development of an algorithm that uses cost-effective photogrammetry (Moon et al., 2019), i.e., RGB images, depth data and camera positions, to automatically detect relevant objects within a building and predict the relations between these objects. The algorithm should yield a graph network, where nodes represent objects and edges represent physical connections between objects. As the main use of this pipeline is for high stakes decision making for critical infrastructures, the algorithm design will focus on explainability and interpretability besides accessibility and cost-effectiveness, where possible. While we were able to validate the pipeline on synthetic scenes that mimic the real world, it remains a prototype that requires validation on actual real-world scenes.

This article is structured as follows. Section 2 places our proposed method into context by giving an overview of the related works. Section 3 details the developed graph generation pipeline and the data of the hydraulic systems used as the test environments for validation. Section 4 presents the results of applying the proposed pipeline to two hydraulic systems. Section 5 conducts a sensitivity and runtime analysis to investigate the robustness and practical feasibility of the pipeline. Lastly, Section 6 outlines the strength and limitations of the pipeline and Section 7 draws a brief conclusion.

## 2 RELATED WORKS

Most of the time, a virtual geometric representation of a building or a facility is the starting point of a digital twin. This representation is then enriched with attributes and information from individual objects, sensors and real-time data (Jones et al., 2020; Grieves, 2014). In the last decade, frameworks such as building information modelling (BIM) have been used increasingly in the planning and building of new facilities and can provide the required geometric and attribute data (Ghaffarianhoseini et al., 2017; Borrmann et al., 2018; Lu et al., 2022). While the adoption of building information modelling has grown rapidly in the last decade, it was likely not used for most older existing buildings. In these cases, the first step in building a digital twin is the collection of geometric data, the identification of relevant objects and the extraction of key attributes (Borkowski, 2023).

A popular method for collecting geometric data is the use of 3D laser scans. Laser scanners create a three-dimensional point cloud with a high resolution providing a detailed virtual representation of reality. However, these scanners are expensive and can cost many tens to hundreds of thousands of dollars. They are also heavy and require expensive software for processing the acquired data. Furthermore, specialized training is needed for operation and they struggle to represent reflective surfaces correctly (Moon et al., 2019). An alternative approach is photogrammetry that aims to generate precise 3D models from photographs and usually involve the computation of depth data. Multi-view stereo, for example, uses multiple perspective of a stereo camera or a RGB and a thermal camera to compute the depth information and a 3D scene (Goesele et al., 2006; Vidas et al., 2013), while Structure-from-Motion uses a series of 2D images to estimate the depth data and camera positions (Schönberger and Frahm, 2016). Overall, systems

68 used for photogrammetry cannot achieve the same level of detail and resolution as 3D laser scanners but  
69 are cheaper, more accessible and more mobile.

70 3D laser scanning and photogrammetry provide two different outputs: point clouds and images. Both  
71 present distinct strength and shortcomings as inputs for object detection. Albeit that point clouds have a  
72 high resolution and are very accurate they are also sparse and the point densities can be highly variable  
73 leading to high computational requirements and costs (Zhou and Tuzel, 2018). Furthermore, there are a  
74 limited number of labeled data sets for point clouds available as labelling in three-dimensional space is  
75 challenging (Zimmer et al., 2022). This also makes collecting and labelling custom data sets for training  
76 difficult and time-intensive. Despite of this, point clouds were used in object detection for hydraulic  
77 systems in various articles (Qiu et al., 2014; Kawashima et al., 2014; Cheng et al., 2020; Alex and Stoppe,  
78 2025), while the use of photogrammetry is limited (Hart et al., 2023; Zhao et al., 2025). However, as  
79 object detection on images is computationally cheaper and more training data is available, easier to collect  
80 and label, it lends itself for object detection as part of a graph generation pipeline that aims to be widely  
81 accessible, applicable to different use cases, and time- and cost-effective. Furthermore, models for object  
82 detection on images are generally more researched and thus more mature than their counterparts using  
83 point clouds. This is also reflected in the many models that are available, many of which even offer good  
84 out-of-the-box performance (Redmon et al., 2016; Kirillov et al., 2023; He et al., 2017; Yuan et al., 2021).  
85 In practice, we found that object detection on the many different perspectives of the images was reliable  
86 and results from different view points had the advantage of enabling validation of detections across images.  
87 The latter was especially valuable for featureless objects and instances in which lights and reflections made  
88 object detection challenging as there were multiple opportunities to detect the same object. This decreased  
89 the possibility of erroneous detections. Thus, we identified photogrammetry in combination with object  
90 detection on images as the superior methods for the pipeline presented in this article. While the presented  
91 pipeline is closely linked to multi-view stereo it is not just a geometric 3D representation of a scene but  
92 also aims to encode relational information between objects of the scene in a graph.

93 The prediction of a relational graph of the objects contained an image, also known as scene graph  
94 generation, through graph neural networks has seen increased interest by the deep learning community  
95 in recent years (Shit et al., 2022; Yang et al., 2018; Li et al., 2024; Cong et al., 2023). These approaches  
96 combine the detection of relevant objects in an image with the prediction of relations between the detected  
97 objects and encode both in a graph. Similar to other deep learning methods, these models are black boxes  
98 lacking explainability and interpretability (Buhrmester et al., 2021; Şahin et al., 2025) and although there  
99 are efforts to remedy this in the form of explainable AI (Xu et al., 2019; Zhang et al., 2022; Dwivedi  
100 et al., 2023; Peng et al., 2024), it is questionable if these efforts suffice when it comes to high stakes  
101 decision-making (Rudin, 2019). Furthermore, scene graph generation networks require data and additional  
102 labeling and cannot easily be transferred to other use cases and scenes involving different objects without  
103 collecting new data. For example, many graph generation networks are based on the 3DSSG data set that  
104 contains 1,482 scene graphs with 48k objects and 544k relations (Wald et al., 2019, 2020; Lv et al., 2024;  
105 Yeo et al., 2025). Collecting and annotating a data set of this size for a specific use case is, in practice, at  
106 least impracticable if not infeasible. An alternative to these models is an approach using heuristics and rules  
107 based on which relations between objects are inferred. Letting the user define a custom set of rules gives  
108 them full control and enables them to tailor the method to a specific application or transfer it to another  
109 without the need of collecting additional training data. While there is some initial manual work involved in  
110 setting up the rules, it is likely negligible compared to the effort of collecting and labelling data for the  
111 graph neural networks. This article chooses the latter approach due to its flexibility and cost-effectiveness  
112 but mainly because the rules make the inner workings of the algorithm transparent and explainable which

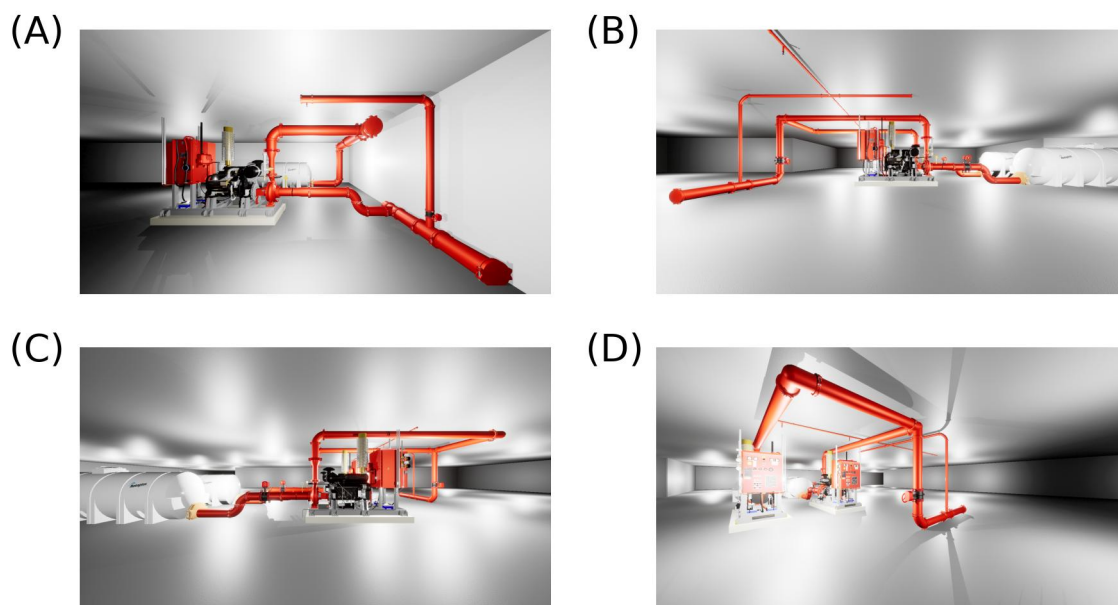


**Figure 1.** Synthetic hydraulic systems. (A) shows system 1 consisting of pipes, one pump, one tank, one valve and one sprinkler. (B), (C) and (D) show system 2 consisting of pipes, two pumps, two tanks, three valves and four sprinklers.

113 is essential for high stakes decision-making as it is required in critical infrastructure (Rudin, 2019). The  
114 process of defining these rules and their requirements are discussed in Section 3.2.3.

### 3 MATERIALS AND METHODS

#### 115 3.1 Data

116 The nature of critical infrastructures prohibits the use of images and data collected at the actual real-world  
117 sites due to security concerns. Thus, we implement virtual representations mimicking the most important  
118 characteristics of their real-world counterparts in Unreal Game Engine 5 (Epic Games, 2022c). We chose  
119 the Unreal Engine as it allows for rapid generation of realistically rendered scenes and contains tools to  
120 provide global dynamic illumination (Epic Games, 2022a), rendering of meshes with arbitrary resolution  
121 (Epic Games, 2022b) and scripted capturing of realistic images in combination with segmentation masks.  
122 We use Colosseum (Codex Labs, 2022), a fork of AirSim (Shah et al., 2017), to simulate cameras in the  
123 Unreal Engine allowing us to produce RGB images and depth data along with the intrinsic and extrinsic  
124 camera parameters, such as the position and orientation of the camera at the time of taking the images.  
125 While real-world testbeds are preferable, the realistic results of the Unreal Engine strike a good balance  
126 between accessibility and an accurate representation of the real world.

127 This paper focuses on the graph generation of hydraulic systems by investigating two test environments.  
128 Hydraulic system 1 consists of a pump, a tank, a valve, a sprinkler and pipes as shown in Figure 1 (A).  
129 Hydraulic system 2 increases the complexity by adding another pump and tank, two valves and three  
130 sprinklers to the design. This system is shown from multiple perspectives in Figure 1 (B), (C) and (D).  
131 Pipes, pumps, tanks, valves and sprinklers are the only objects in these test environments. It should be  
132 noted that the distinct color of the pipes compared to the floor, walls and ceiling is chosen for illustrative  
133 purposes only. The components of the pipeline, such as the models used for object detection, are not reliant

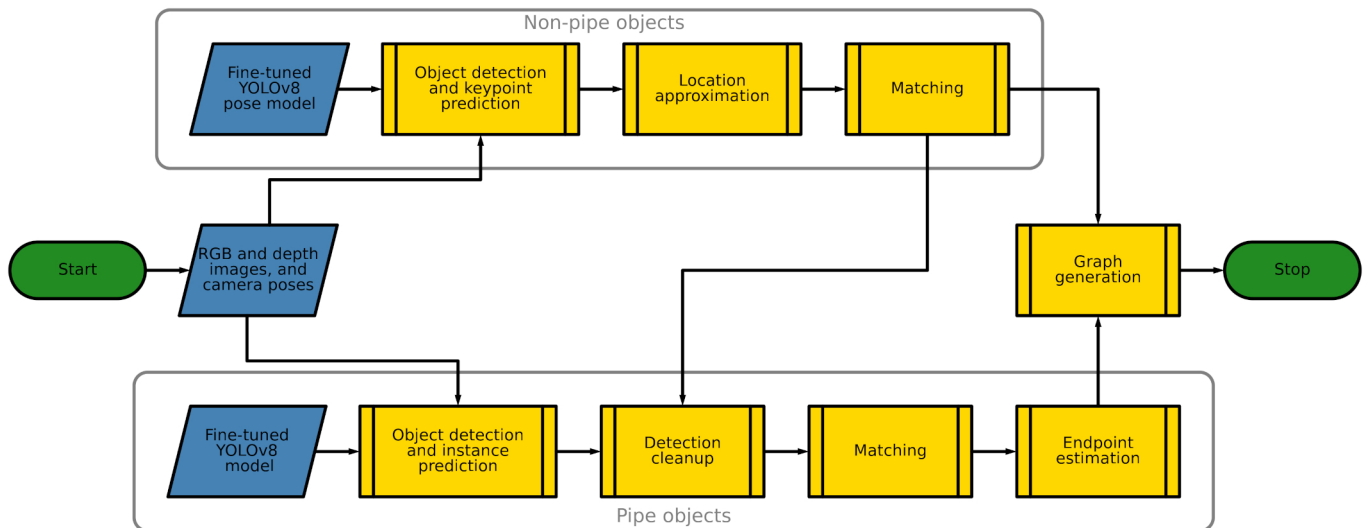


**Figure 2.** Flowchart of the graph generation pipeline. Pipe and non-pipe objects are treated differently and are combined in the 'Graph generation' module.

134 on the color of the pipes as they were trained and tested on a wide range of different color and texture  
 135 compositions. We use domain randomization to randomly generate different color and texture combinations  
 136 for the pipe objects and use them to produce a diverse set of training images via the Unreal Engine for  
 137 fine-tuning YOLOv8 as outlined in more detail in Schreiber et al. (2024).

138 Data for hydraulic system 1 comprises 16 RGB and depth image pairs with a resolution of  $1920 \times 1080$   
 139 pixels and a field-of-view of 114 degrees. For the more complex hydraulic system 2, we stock up the  
 140 number of RGB and depth image pairs to 29 with identical resolution and field-of-view.

141 The training data for YOLOv8 consists of photos of hydraulic systems taken with a Canon EOS 7D SLR  
 142 camera at a resolution of  $6000 \times 4000$  pixels and synthetic images generated with Unreal Engine 5 as  
 143 non-interlaced 8-bit RGBA images with a resolution of  $1920 \times 1006$  pixels.

## 144 3.2 Pipeline

145 The graph prediction pipeline is structured as shown in Figure 2. The pipeline differentiates between  
 146 pipe and non-pipe objects and processes them with two distinct approaches. Both use RGB images, depth  
 147 data and camera poses including the camera position and camera orientation of the individual images and  
 148 a fine-tuned YOLOv8 model (Redmon et al., 2016). While we chose YOLOv8 for object detection, the  
 149 pipeline in this study does not require the use of YOLOv8. The detection model is solely an input of the  
 150 pipeline and can be replaced with any preferred model. We decided to use YOLOv8 as it is an established  
 151 model that does not require a large data set for fine-tuning the pre-trained model to a new detection task  
 152 as it is the case for vision transformers (Dosovitskiy et al., 2021). It also provides versions for instance  
 153 segmentation and keypoint prediction that are used as described in the following sections.

### 154 3.2.1 Non-pipe objects

155 Non-pipe objects are processed using a fine-tuned YOLOv8 pose model (Redmon et al., 2016) that detects  
 156 the pumps, tanks and valves within the images and predicts one keypoint for tanks and two keypoints for  
 157 pumps and valves. These keypoints represent the connection points of the tanks, valves and pumps with  
 158 other objects, such as pipes. The largest YOLOv8 architecture pre-trained on the COCO data set (Lin et al.,

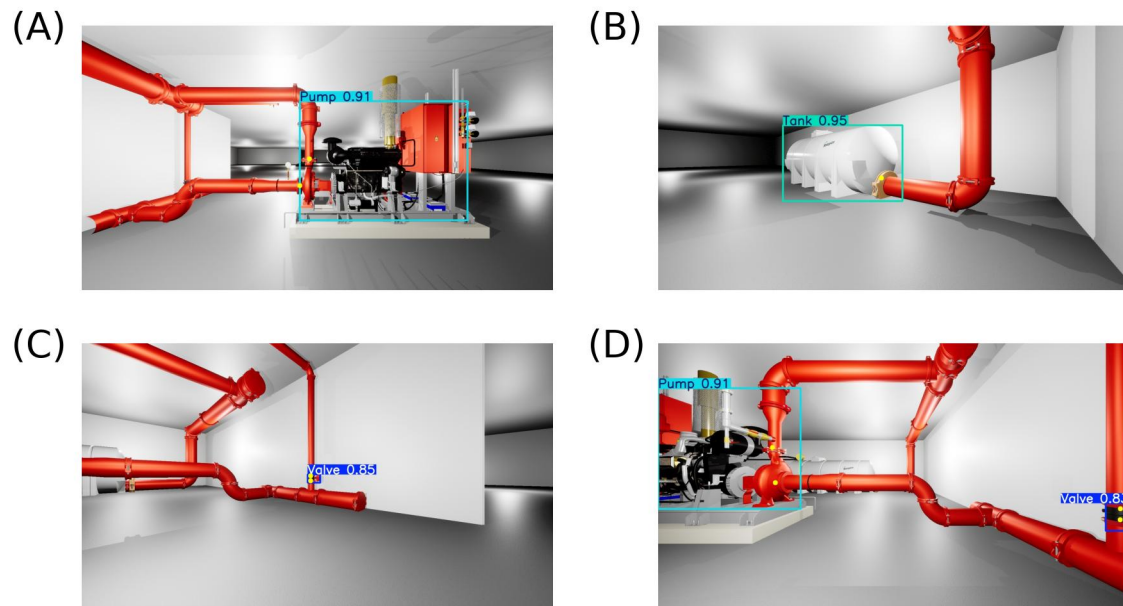


**Figure 3.** Object detection of pumps, tanks and valves including one keypoint for tanks and two keypoints for pumps and valves. Bounding boxes indicate detected objects with class label and class confidence score. Keypoints are indicated by yellow dots.

159 2014) was chosen as a foundation. This model was fine-tuned using a data set consisting of 526 images,  
 160 with 280 being real-world RGB images and the remaining 246 being synthetically created using Unreal  
 161 Engine 5 (Epic Games, 2022c). The training was conducted for 150 epochs using the Adam optimizer  
 162 and a learning rate of  $10^{-4}$ . Figure 3 shows predictions of the model for four images. Detections for an  
 163 object consist of a bounding box with a class label and a class confidence score, and keypoints plotted in  
 164 yellow. For example, Figure 3 (A) shows a pump detected with a confidence of 91 % and two keypoints  
 165 indicating the connection points with the neighboring pipes. YOLOv8 uses Non-Maximum-Suppression  
 166 (NMS) to discard redundant detections by only using bounding boxes with the highest confidence score  
 167 and dismissing other overlapping bounding boxes with lower confidence scores.

168 The second module in the 'Non-pipe objects' branch of the pipeline aims to approximate the location of  
 169 the objects within the bounding boxes. While it would be possible to use an instance segmentation method  
 170 to get exact masks of the objects (similar to the segmentation used for the pipes in Section 3.2.2), exact  
 171 masks are not required for the pipeline to achieve satisfying results. Hence, we opt for an approximation of  
 172 object masks sparing us time-consuming instance labelling of the more intricate non-pipe objects. The main  
 173 objective of the location approximation is to delete any background pixels within the predicted bounding  
 174 boxes, leaving us with only pixels belonging to the object. Experimentation showed that we can achieve  
 175 this objective by chaining three methods together: (i) We disregard any pixels with depth values larger than  
 176 the median of all depth values within a bounding box. This eliminates the majority of the background. (ii)  
 177 We refine the mask by projecting the remaining pixels to a point cloud down-sampled to one voxel per  
 178  $\text{cm}^3$  and removing any statistical outliers (voxels that deviate more than one standard deviation from a  
 179 neighborhood consisting of the closest 25 % of all other voxels). (iii) Finally, we employ Density-Based  
 180 Spatial Clustering of Application with Noise (DBSCAN) to approximate the location of the object (Ester  
 181 et al., 1996; Schubert et al., 2017). We setup DBSCAN such that points that are less than 2 cm apart are  
 182 assigned to a cluster. Finally, the largest cluster is taken as the approximated location.

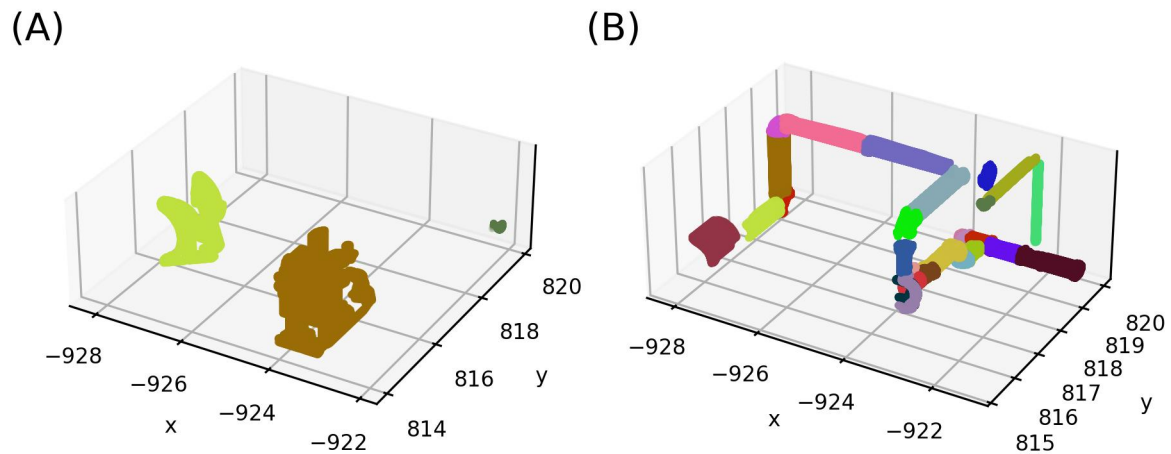


**Figure 4.** Object matching across individual images. (A) shows the matched objects of a pump, a tank and a valve and (B) shows the matched pipe objects. Each color indicates a distinct object.

183 The last module in processing the non-pipe objects matches identical detections across images and  
 184 combines information in one final object. In this step, the approximated locations of merged objects  
 185 are combined and their endpoints (predicted via the keypoints) are averaged. Before averaging, possible false  
 186 predictions are disregarded via statistical outlier removal of keypoints that deviate more than two standard  
 187 deviations from all keypoints. Two objects from different images are merged if the following rule for the  
 188 pairwise distances  $\mathbf{d}$  between all their voxels is true:

$$\frac{\sum_{i=1}^n \mathbb{1}_{\{d_i < np\_max\_distance\}}}{n} > np\_min\_percentage,$$

189 where  $n$  is the number of elements of vector  $\mathbf{d}$ , and  $np\_max\_distance \in (0, \infty)$  and  
 190  $np\_min\_percentage \in [0, 1]$  specify the maximal distance in meters between two object points to be  
 191 considered a match and the minimal percentage of matched points required for two objects to be matched,  
 192 respectively.  $\mathbb{1}$  is the indicator function that returns 1 if a distance  $d_i$  is smaller than  $np\_max\_distance$   
 193 and 0 otherwise. Thus, two objects are merged if the fraction of the number of pairwise distances smaller  
 194 than  $np\_max\_distance$  and the number of all pairwise distances is larger than  $np\_min\_percentage$ .  
 195 The pipeline sets  $np\_min\_percentage$  to 0.1 requiring two objects to have at least 10 % of points  
 196 within  $np\_max\_distance$  meters. Thus, whether two objects are merged is mainly controlled by setting  
 197  $np\_max\_distance$ . Figure 4 (A) shows three matched non-pipe objects from a total of 16 images using the  
 198 approach outlined in this section.

### 199 3.2.2 Pipe objects

200 The pipeline uses the YOLOv8 model (Redmon et al., 2016) to predict instance segmentations for  
 201 individual pipe elements. This model is pre-trained on the instance segmentation images of the COCO  
 202 data set (Lin et al., 2014). Since the instance segmentation task is more complex compared to the pose  
 203 estimation task, the largest architecture of YOLOv8 and a data set consisting of 1,030 images are applied.  
 204 The pre-trained model is fine-tuned with 280 real-world RGB and 750 Unreal Engine images for 200  
 205 epochs and optimized using Adam with a learning rate of  $10^{-4}$ . Figure 5 shows predictions for four images.



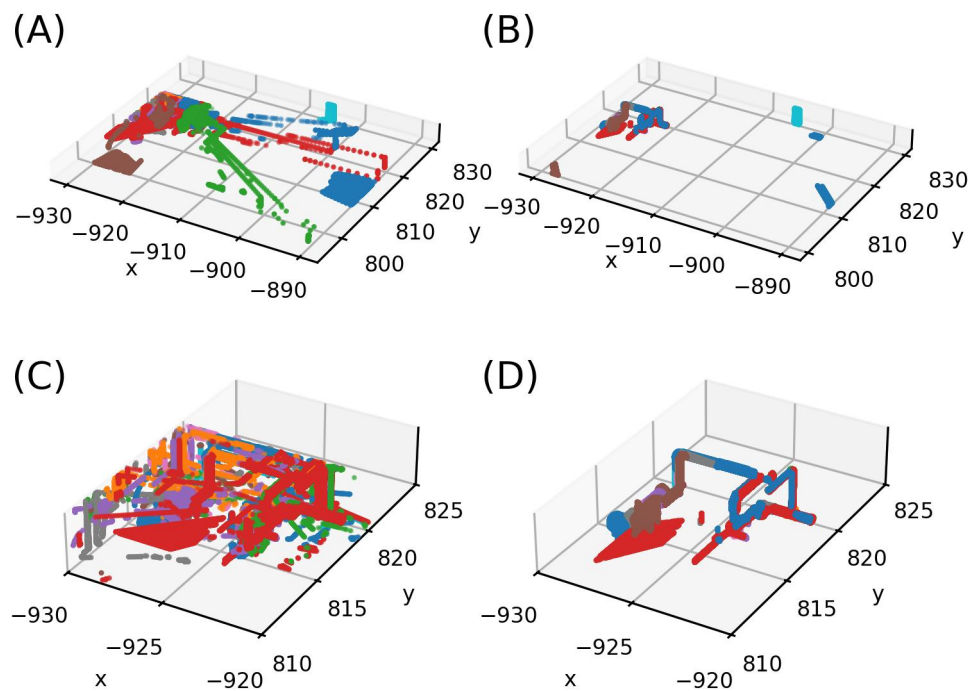


**Figure 6.** Cleanup of pipe segmentations projected to world view. (A) shows the initial segmentations, while (B) shows segmentations after cleanup. (C) and (D) are a zoomed-in version of (A) and (B). Each color indicates segmentations from an individual image.

229 After cleaning the detections, the remaining pipe masks are matched across the images. The matching  
 230 process consists of two steps. First, each mask is projected onto all other images and the intersection with  
 231 the masks of these images is computed. This is done for all masks and all images. This process is depicted  
 232 for one image pair in Figure 7, where (A) shows the target image on which masks of the source image  
 233 (B) are projected. (C) shows this projection with pipe elements of the target image now displayed in gray.  
 234 (C) shows that at least three pipe elements of the source image are projected onto pipe elements of the  
 235 target image. This will result in a positive intersection area for these pipe element pairs indicating possible  
 236 matches. Projections are based on the pinhole camera model (Hartley and Zisserman, 2003). Second, to  
 237 validate that the overlapping masks are actual matches, they are projected into three-dimensional world  
 238 view, voxels are down-sampled to one  $\text{cm}^3$  and DBSCAN (Ester et al., 1996; Schubert et al., 2017) is used  
 239 to find distinct clusters that are at least 10 cm apart. Each of these clusters is subsequently considered an  
 240 individual object.

241 While the endpoints of the non-pipe objects are predicted by YOLO as outlined in Section 3.2.1, the  
 242 YOLOv8 model used for instance segmentation does not predict keypoints. Thus, an approximation of the  
 243 endpoints for the pipe objects is required. Pipe objects can be classed into two categories: straight pipes and  
 244 non-straight pipes, such as bent pipes and T-fittings. We differentiate between these classes by computing a  
 245 rotated bounding box around the objects and comparing its longest side against its shorter sides. If the ratios  
 246 of  $\frac{\text{length of long side}}{\text{length of short side}}$  are larger than hyperparameter  $p\_threshold \in [0, \infty)$ , the pipe is classed as straight. If  
 247 the ratios are equal or smaller than this hyperparameter, the pipe is classed as non-straight. Voxels are  
 248 binned along the longest side of the bounding box and the mean of all voxels within the first and the last bin  
 249 are used as the two endpoints of the pipe. Figure 8 (A) and (B) show wireframes of the hull of two straight

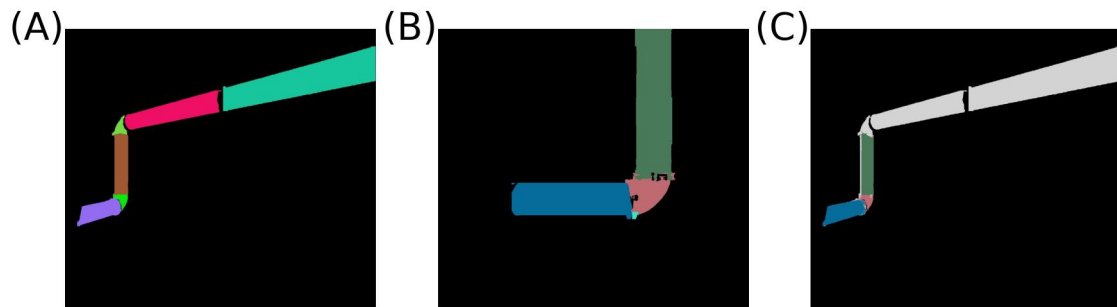


**Figure 7.** Projection of segmented pipes. (A) is the target image on which segmented pipes of the source image (B) are projected. (C) shows the projected segmentations from (B) in color on the segmentations of (A) in gray.

250 pipes in blue and the approximated endpoints as red spheres. For the non-straight pipes, it is generally more  
 251 challenging to find an appropriate heuristic that gives satisfying results. Thus, we begin by computing the  
 252 centroid of the object and place it towards the most relevant neighboring object. In detail, we find the object  
 253 that has the highest number of voxels within  $p\_max\_distance \in (0, \infty)$  meters of the hull of the pipe  
 254 object and use the linear combination  $(1 - p\_w) \times centroid + p\_w \times neighbor$  to find the final position  
 255 of the endpoint.  $p\_max\_distance$  is the maximal distance in meters around the pipe objects hull in which  
 256 other objects are considered and  $p\_w \in [0, 1]$  controls how far a centroid is pulled towards the other objects.  
 257 The pipeline sets  $p\_w = 0.3$  which slightly nudges the endpoints towards the objects neighboring in close  
 258 proximity. This process is executed twice for each centroid yielding two endpoints for each pipe object.  
 259 Figure 8 (C) and (D) show two examples of two 90 degree bents. While this method provides satisfying  
 260 results for most objects, it struggles with pipe objects that have an ambiguous shape (Figure 8 (E) and (F))  
 261 as discussed in detail as part of the limitations in Section 6.

### 262 3.2.3 Connection prediction and Graph generation

263 The processes for non-pipes (Section 3.2.1) and for pipes (Section 3.2.2) yield endpoints for each object  
 264 that can be used to predict how individual objects are connected and how all objects that form an entire  
 265 hydraulic system relate to each other. The whole scene can effectively be described as a relational graph in  
 266 which objects are nodes and object connections are indicated by edges between these nodes. The idea of  
 267 the graph generation process is to first create a initial graph with probable connections and then refine this  
 268 graph by defining and enforcing a set of rules. This process is depicted in Figure 9.

269 The initial graph is generated by computing the pairwise distances between the endpoints of all objects  
 270 and iteratively connecting objects, i.e., drawing edges between nodes weighted by their respective pairwise  
 271 distance, starting with the smallest distance. Nodes are iteratively connected until all remaining distances  
 272 between endpoints are larger than the hyperparameter  $graph\_max\_distance \in (0, \infty)$ . Two individual  
 273 objects are restricted to a single connection. An example of an initial graph is shown in Figure 9 (A).

274 The initial graph is then refined by defining a set of rules and enforcing them. This means that edges  
 275 breaking at least one of the rules are deleted from the graph, beginning with the edge with the largest  
 276 distance, until no further rule violation exists. For the hydraulic systems considered in this articles, the  
 277 following rules are enforced:

- 278 - **Rule 1:** Pumps and valves are limited to a maximum of two connections, tanks to a maximum of one  
 279 connection.

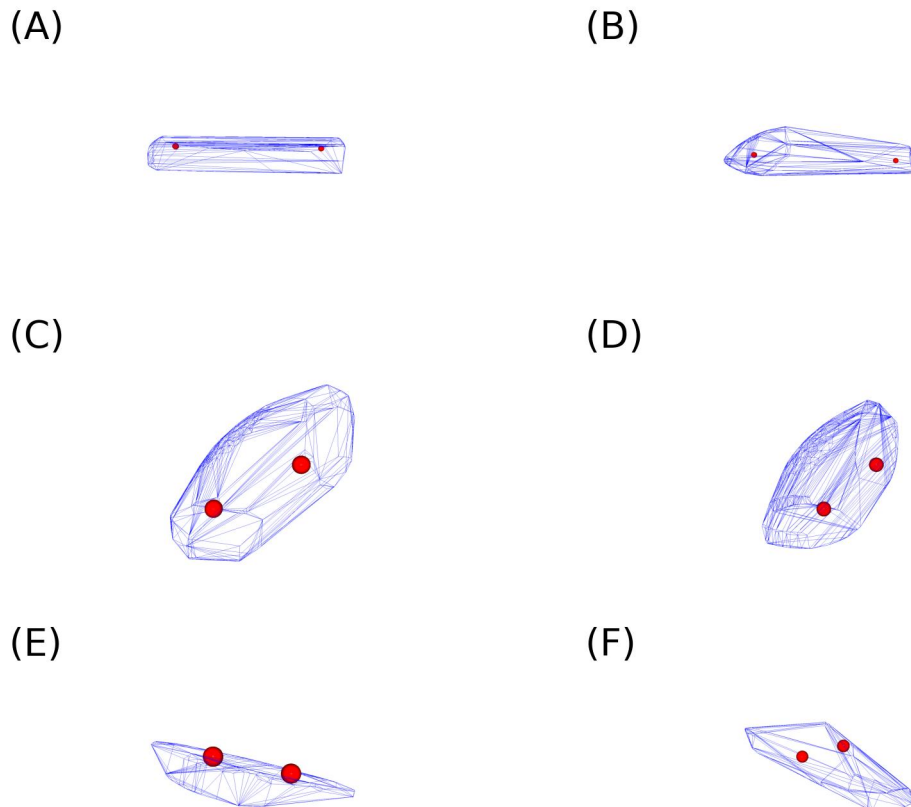


**Figure 8.** Endpoint approximation of pipe elements. Blue lines are a wireframe representation of the pipe elements while red spheres indicate approximated endpoints. (A) and (B) show approximations for straight pipe elements, (C) and (D) for bent pipe elements, and (E) and (F) for ambiguous pipe elements.

- 280 - **Rule 2:** Pipes are limited to a maximum of three connections.
- 281 - **Rule 3:** Neighbors of the same non-pipe object cannot be connected.
- 282 - **Rule 4:** Single nodes are not allowed.
- 283 - **Rule 5:** Cycles are not allowed.
- 284 - **Rule 6:** Pipes directly connected to pumps are classed as Reducer/Expander.
- 285 - **Rule 7:** Pipes with three neighbors are classed as PipeCrossing.

286 The graphs in Figure 9 (B) through (H) display the results after enforcing each of the rules. While the  
 287 initial graph (A) is convoluted and no clear system can be identified, the graph takes a more realistic shape  
 288 with each step until its final shape is reached at (F). After that updates only address the type of the existing  
 289 nodes. Straight and bend pipes are assigned type 'Pipe', T-fittings are assigned type 'PipeCrossing', and  
 290 pipes adjacent to pumps are assigned type 'Reducer/Expander'. The diameter of the latter decreases or  
 291 increase in the direction of the flow to facilitate proper functioning of the connected pump. The final graph  
 292 is thoroughly discussed in Section 4.1.

293 While these rules work well for the hydraulic system considered in this paper, they are not appropriate or  
 294 sufficient for every type of structural critical infrastructure. However, the pipeline makes it straightforward

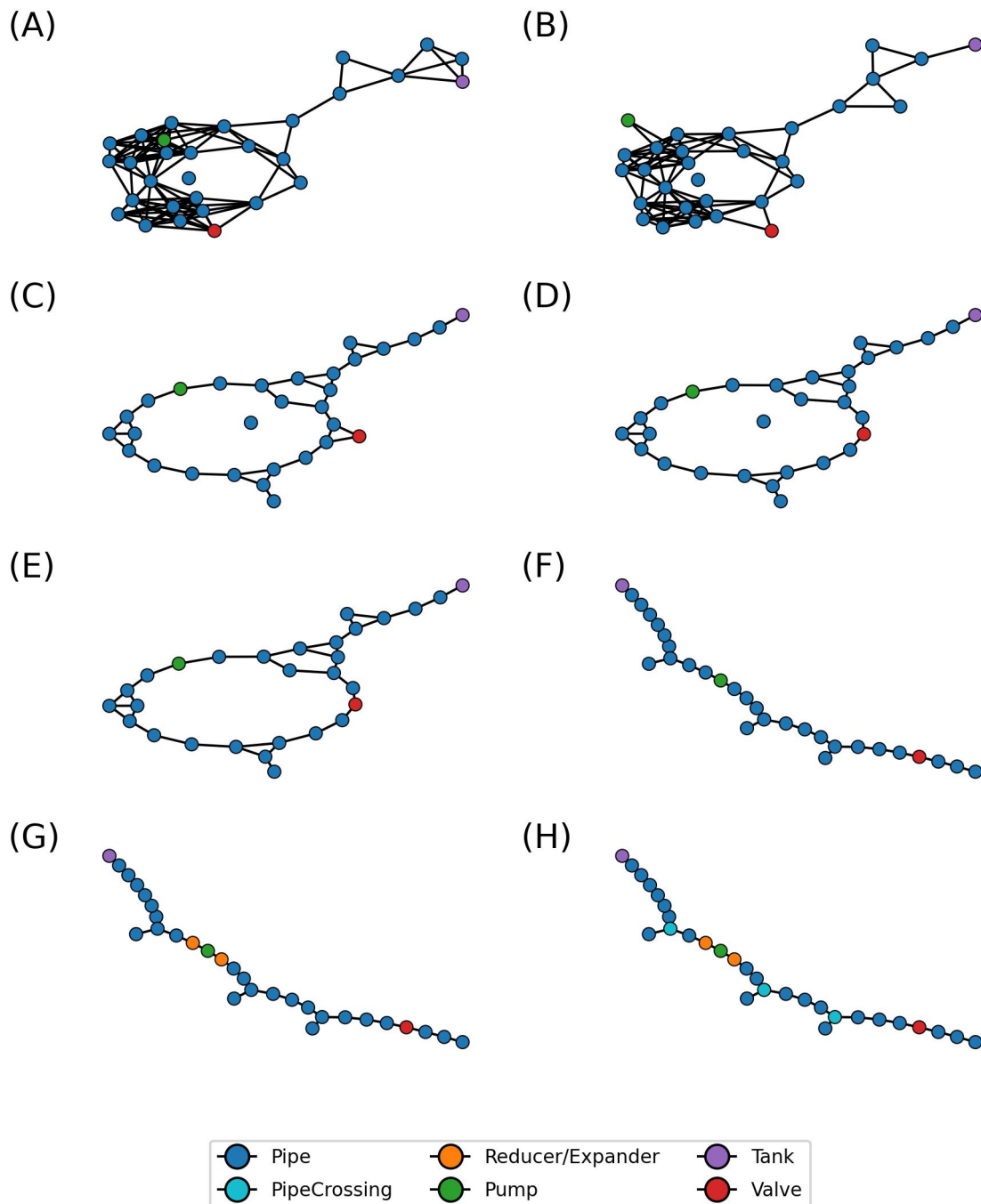


**Figure 9.** Graph generation. (A) shows the initial graph based on distance between endpoints, and (B) through (H) show graphs enforced by the individual rules discussed in Section 3.2.3.

295 to add new rules. Each rule is essentially a function that takes the current graph as the input and returns the  
 296 adjusted graph as the output. The way in which the function alters the graph is defined by the rule itself.  
 297 For Rule 1, for example, the function gathers all pumps and valves, counts the connections of each and  
 298 deletes edges beginning with the largest distance for instances where one pump or valve has more than two  
 299 connections. Adding a new rule requires defining a new function and inserting it at the appropriate position  
 300 relative to the other rules. An advantage of implementing rules as simple functions is that their behaviour  
 301 can easily be validated and scrutinized by feeding them a graph that breaks the specific rule and observing

**Table 1.** Parameters used in the prediction of hydraulic systems 1 and 2.

Parameter	Module	System 1	System 2
<i>np_max_distance</i>	Non-pipe matching	0.75	0.75
<i>p_matching_min_overlap</i>	Pipe matching	0.70	0.70
<i>p_threshold</i>	Pipe endpoint estimation	2.00	2.00
<i>p_max_distance</i>	Graph generation	1.50	1.50
<i>graph_max_distance</i>	Graph generation	1.50	1.50

302 if the returned graph no longer includes rule violations. This makes the rules transparent and their behavior  
 303 predictable. Thus, this approach is easy to interpret, particularly, when compared to methods relying on  
 304 deep learning black boxes as introduced in Section 2.

## 4 RESULTS

305 This section presents the results for two hydraulic systems generated by the Unreal Engine 5 (Epic  
 306 Games, 2022c), as discussed in Section 3.1. We compare the predicted graph against the ground truth  
 307 in Figures 10 and 11 and highlight differences through three-dimensional plots depicting the individual  
 308 objects of the systems in Figure 12. Neighboring connected pipe objects are contracted in these figures to  
 309 make the comparison, both qualitative and through computing the graph edit distance Gao et al. (2010)  
 310 as a quantitative metric, more convenient. Furthermore, we maintain the position of the pipes to enable  
 311 downstream simulation. Hence, only the visual appearance of the graphs changes and no information about  
 312 the actual 3D system is lost. This is shown in Figure 12 where each individual object is retrieved from the  
 313 graphs. Values of the hyperparameters used to generate these results are shown in Table 1. Section 3.2  
 314 describes all hyperparameters in detail and Section 5 discusses how hyperparameters were selected and  
 315 conducts a sensitivity analysis. Potential implications of these differences are addressed in Section 6.

### 316 4.1 Hydraulic system 1

317 Hydraulic system 1 consists of one tank, one pump, one valve and one sprinkler as well as three T-fittings  
 318 as displayed in the ground truth graph in Figure 10 (A). Figure 10 (B) shows the graph predicted by the  
 319 pipeline detailed in Section 3.2 with errors indicated by red edges. The overall shape of the graphs is  
 320 almost identical. The three T-fittings (displayed as 'PipeCrossing') are present in both graphs and the graph  
 321 starts with a tank on one end, followed by the pump and valve and pipe elements in between each of the  
 322 non-pipe objects. Solely the sprinkler is not included. However, this is not a shortcoming of the pipeline  
 323 itself but rather the sprinklers in the images of the specific data set are too small to be detected by the  
 324 fine-tuned YOLOv8 model (Redmon et al., 2016). The graph edit distance Gao et al. (2010) using a cost of  
 325 1 for deletion and insertion and a cost of 2 for substitution equates to 4. This indicates a high similarity  
 326 between the ground truth and the prediction. Figure 12 (A) shows some errors in the prediction of the  
 327 individual pipe objects. Particularly, there are instances where two subsequent pipe objects are falsely  
 328 predicted as one pipe object: The gold pipe parallel to the y-axis at ground level at (-924, 819) and the  
 329 olive pipe parallel to the y-axis at ceiling level at (-922, 820), respectively. Both pipes combine a straight  
 330 pipe and a 90 degree bent in one pipe object. Moreover, the plot shows that the tank (bright green object at  
 331 (-928, 817)) is approximated in the correct location but is not detected entirely missing a significant part  
 332 towards the x-axis. Lastly, a pipe object at ceiling level at (-924, 819) is partly missing. Implications of  
 333 these error and mitigation are discussed in Section 6.

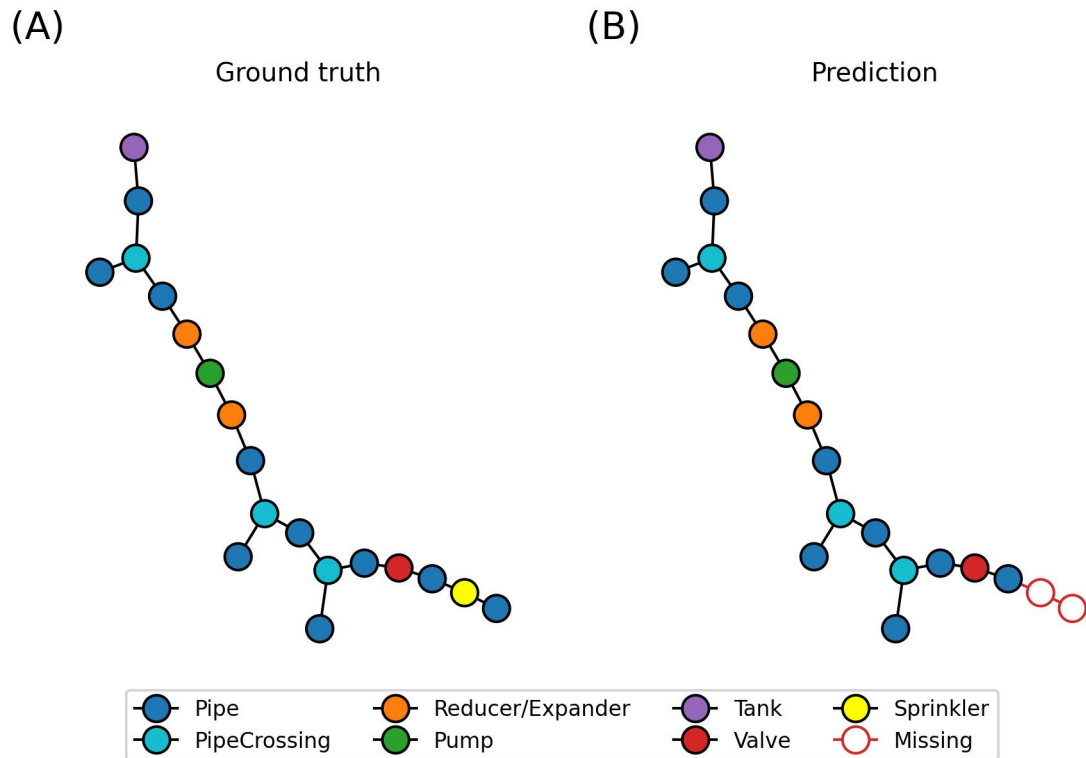


**Figure 10.** Comparison of ground truth (A) to predicted graph (B) for hydraulic system 1.

## 334 4.2 Hydraulic system 2

335 Hydraulic system 2 is more complex than system 1. It consists of two tanks, two pumps, three valves  
 336 and four sprinklers separated by various pipes and T-fittings. The system has an X-shape with the tanks  
 337 and pumps on one side and the sprinklers on the other as shown in the ground truth in Figure 11 (A).  
 338 The prediction (B) of the side with the pumps and tanks only shows a minor difference in the number  
 339 of predicted pipe elements between the valves and the pumps. This difference is due to the detection of  
 340 extra pipe elements by YOLOv8 (Redmon et al., 2016), as discussed in Section 3.2.2, and the consequent  
 341 incorrect matching within the pipeline. In Figure 12, these errors manifest, for example, as the small  
 342 additional pink pipe element at (0, -6). The opposite side with the sprinkler system of the graph in Figure 11  
 343 (B) is not connected to the graph due to an undetected thin vertical pipe at (-6, -8) in Figure 12 (B). See  
 344 Figure 1 (B) for comparison, where the thin vertical pipe can be seen on the left. Similar to system 1, the  
 345 sprinklers objects were too small to be detected by YOLOv8 and thus are neither included in the graph nor  
 346 the three-dimensional representation of the system. The GED Gao et al. (2010) for the entire hydraulic  
 347 system 2 is 22. Considering that the reason for the missing sprinklers is not the pipeline itself but rather  
 348 the detection model which is just an input to the pipeline and can be replaced with any prediction model,  
 349 disregarding the errors caused by the missing sprinklers might be a more accurate metric. In this case the  
 350 GED drops to 10.

## 5 SENSITIVITY ANALYSIS AND RUNTIMES

351 In this section, we want to outline how good values for the hyperparameters listed in Table 1 can be selected  
 352 before analyzing the sensitivity of the outcome to changes in these hyperparameters.

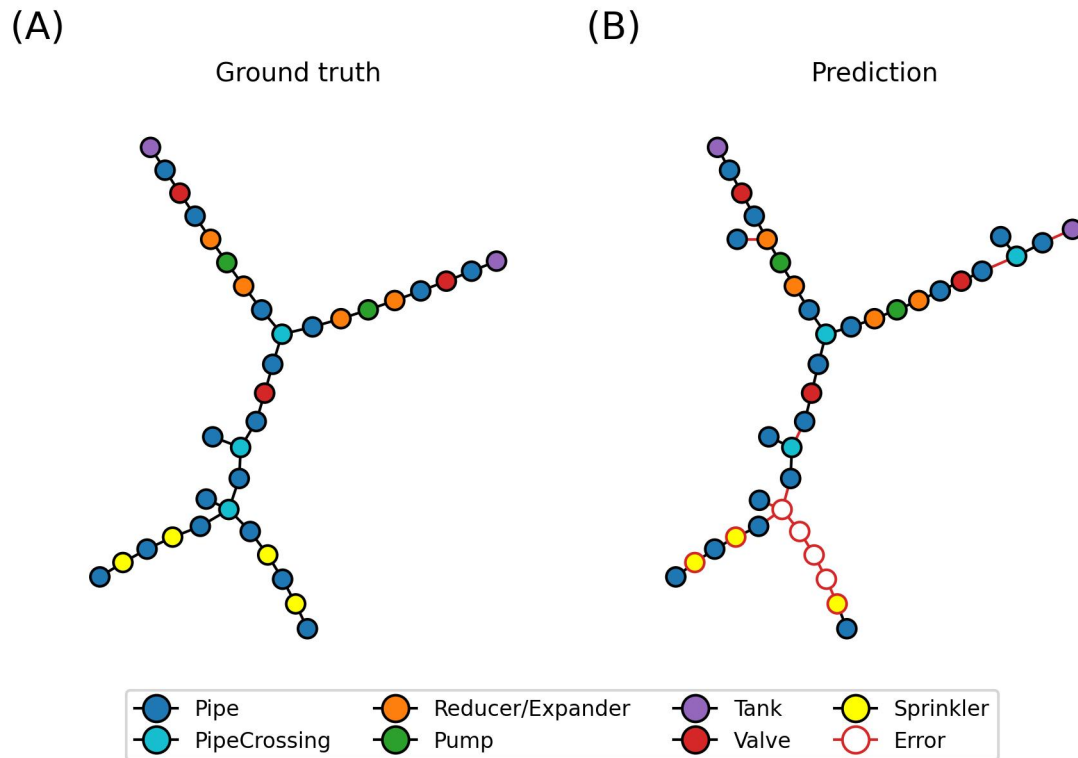


**Figure 11.** Comparison of ground truth (A) to predicted graph (B) for hydraulic system 2.

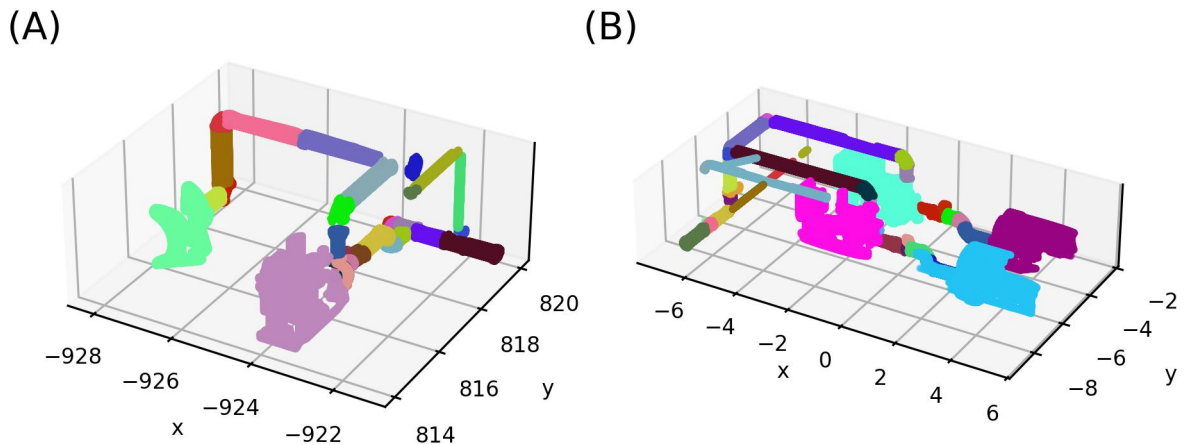


**Figure 12.** Prediction of individual objects for hydraulic system 1 (A) and hydraulic system 2 (B).

353 An advantage of the modular approach presented in Figure 2 is that we can tune the hyperparameters of  
 354 each module individually. For the none-pipe objects, the only hyperparameter to set is *np\_max\_distance*  
 355 which controls the merging of objects detected in multiple images. Particularly, it provides the maximal  
 356 distance in meters that detections can be apart in three-dimensional space to be combined into one object.  
 357 Intuitively, this parameter can be set to just below the minimal pairwise distance between all non-pipe  
 358 objects. Figure 13 shows the final none-pipe objects for different values of *np\_max\_distance*. Evidently,  
 359 if the parameter is too small, one object might be falsely split into multiple objects as is the case for

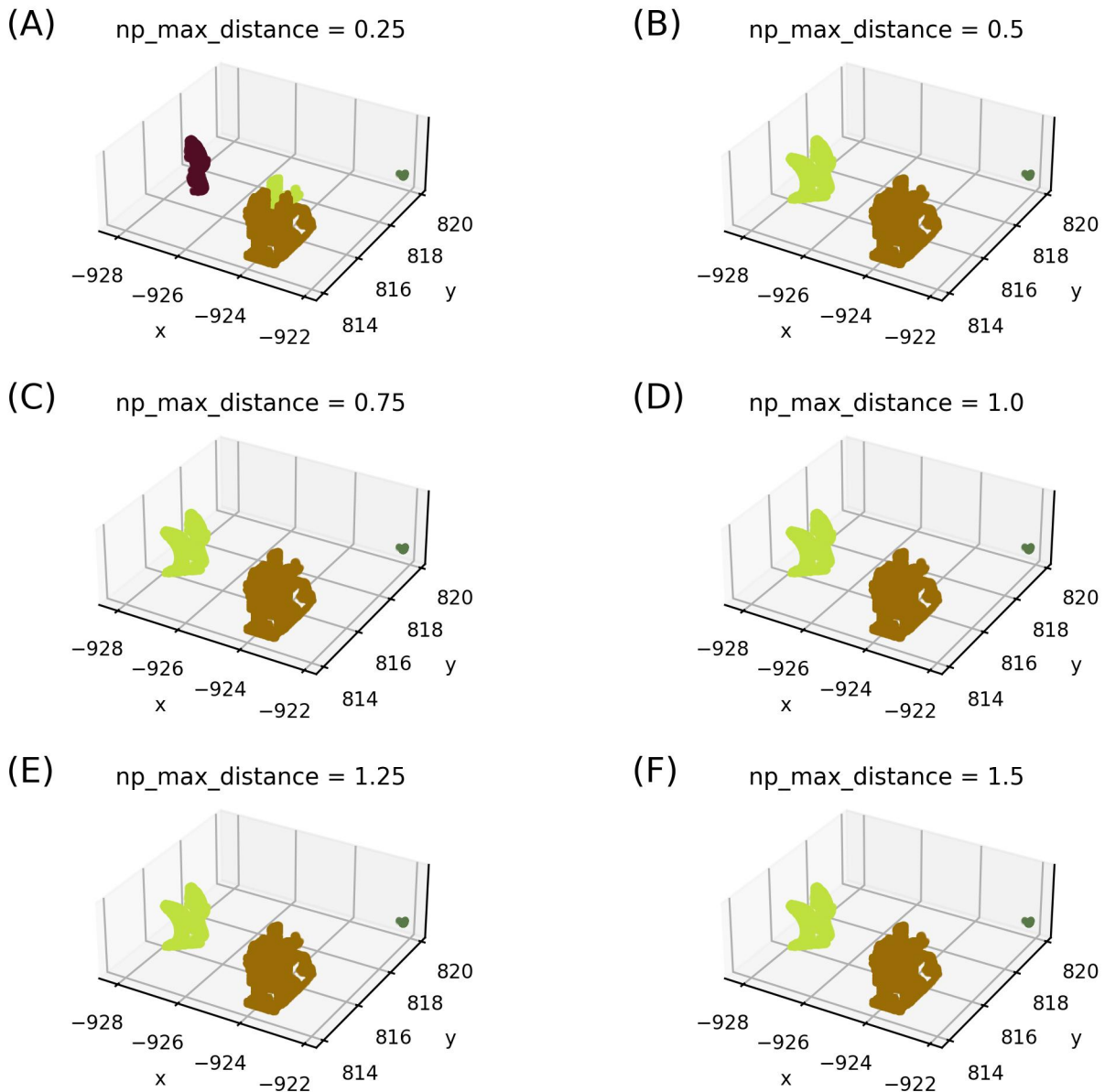


**Figure 13.** Tuning of hyperparameter  $np\_max\_distance$ . Orange points indicate hyperparameters used for hydraulic system 1.

360  $np\_max\_distance = 0.25$  in Figure 13 (A). If the parameter is set too large, multiple distinct object might  
 361 be combined into a single object, however, this is not the case up to the maximum considered distance of  
 362 1.5 meters in Figure 13 (F). Thus, setting the value to a distance that is just below the minimal pairwise  
 363 distance between all non-pipe objects is advisable.

364 The only hyperparameter that requires tuning for processing and matching the pipe objects is  
 365  $p\_matching\_overlap$  which controls the minimal required overlap of two masks to be matched together as  
 366 shown in Figure 7. Figure 14 shows results for a range of  $p\_matching\_overlap$  values, where each color  
 367 indicates one pipe object. If the parameter is set too low, many pipe objects will erroneously be matched  
 368 together. If the parameter is set too high, individual pipe elements might be split into multiple objects.  
 369 When setting this parameter, it is easiest to plot a range of different values and select the highest value for

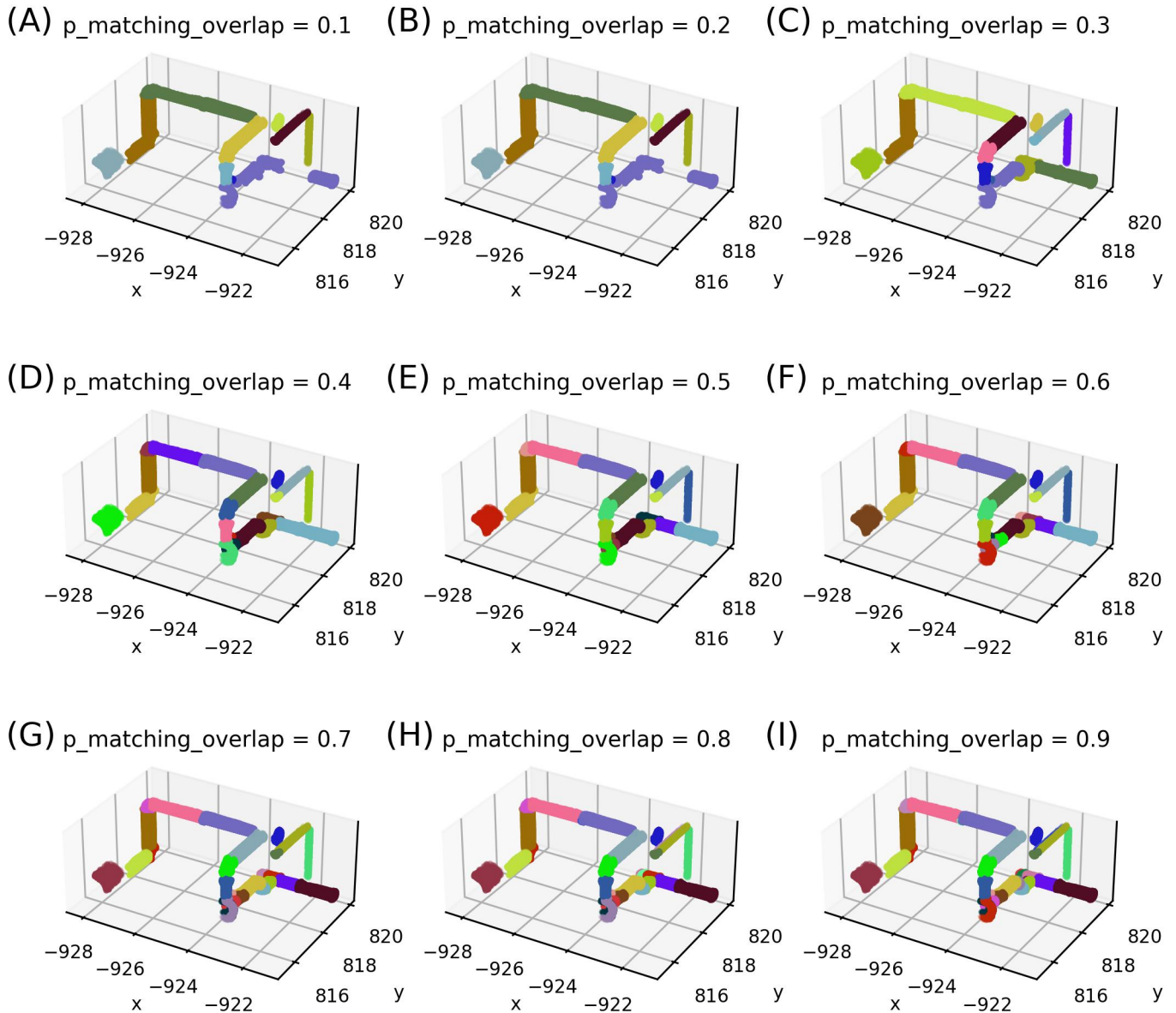


**Figure 14.** Tuning of hyperparameter  $p\_matching\_overlap$ . Orange points indicate hyperparameters used for hydraulic system 1.

370 which individual pipe elements are not split into multiple objects. In this case  $p\_matching\_overlap = 0.7$   
 371 meets this criteria. This process is feasible as the pipe matching process takes an average of 14.55 seconds  
 372 to complete (as discussed later in this section) and thus enables rapid experimentation.

373 When setting the remaining three hyperparameters  $p\_threshold$ ,  $p\_max\_distance$  and  $graph\_max\_distance$   
 374 the same process as before can be applied as approximating the endpoints and generating the graph  
 375 only takes 1.64 seconds. We chose the graph in Figure 10 as the best performing solution which uses  
 376  $p\_threshold = 2.0$ ,  $p\_max\_distance = 1.5$  and  $graph\_max\_distance = 1.5$ . To make this approach of  
 377 setting the hyperparameters feasible for large scenes, hyperparameter tuning can either be performed on  
 378 a small area of the scene and then used for the full scene, or it can be performed on one scene and then

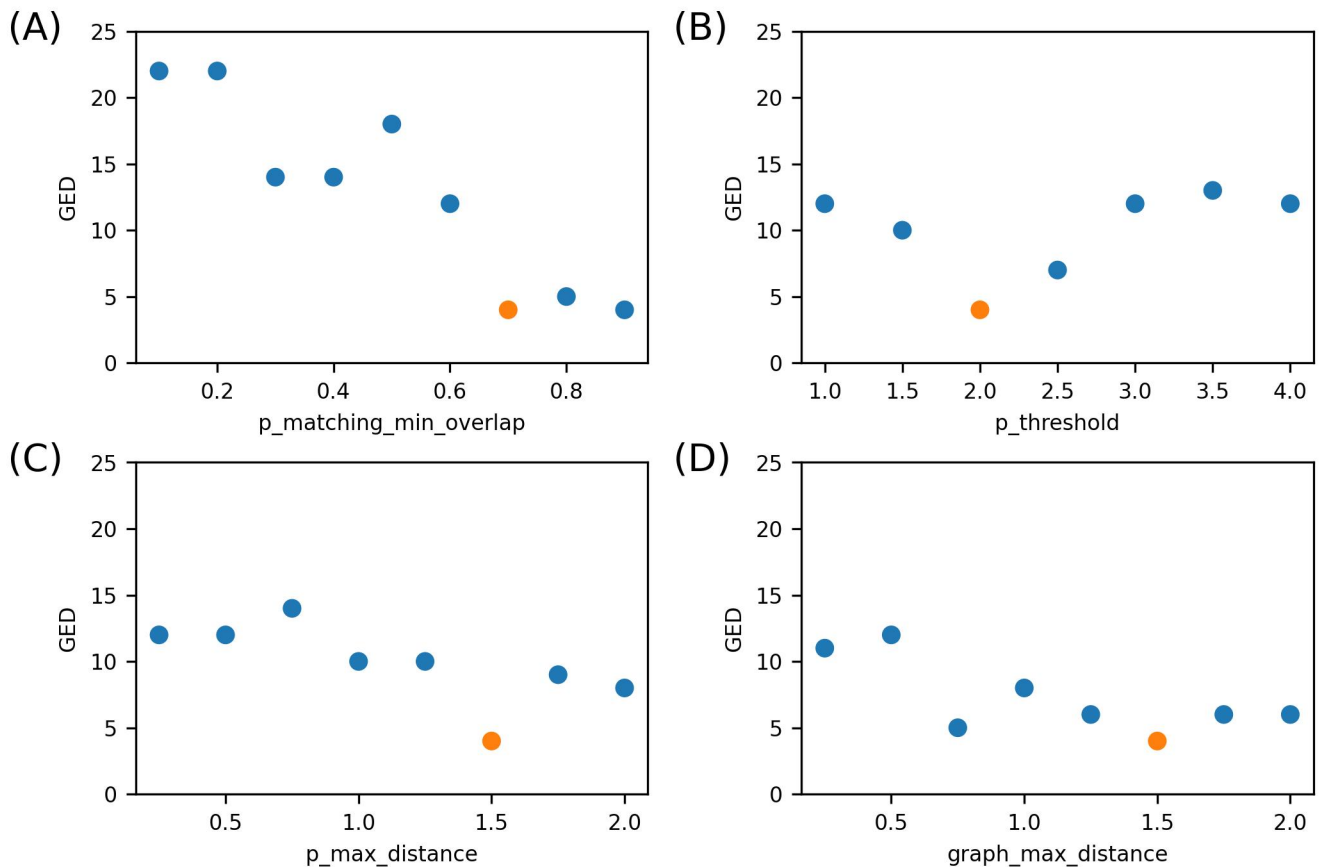


**Figure 15.** Sensitivity analysis of pipeline hyperparameters. Orange points indicate hyperparameters used for hydraulic system 1.

379 transferred to another. We opted for the latter option and tuned the hyperparameters on system 1 and  
 380 applied the pipeline using the same hyperparameters to system 2.

381 Furthermore, we conducted a sensitivity analysis of the hyperparameter to give further guidance on how  
 382 changes affect the results. Figure 15 provides the graph edit distance (GED) (Gao et al., 2010) for four  
 383 hyperparameters over a range of different values, where the orange circles display the hyperparameters  
 384 used for the results presented in Section 4. The GED is computed with an insertion and deletion cost of 1  
 385 and a node substitution cost of 2. We only adjust the value for the displayed hyperparameter while the  
 386 others remain as given in Table 1. The analysis shows that values above  $p\_matching\_overlap = 0.6$  and  
 387  $graph\_max\_distance = 1.0$  result in similar GEDs, while  $p\_threshold$  and  $p\_max\_distance$  are more  
 388 sensitive to changes displaying optimal values at 2.0 and 1.5, respectively. This indicates that it is advisable  
 389 to set  $p\_matching\_overlap$  and  $graph\_max\_distance$  towards the upper end of the parameter range while  
 390 results profit from a more precise tuning of parameters  $p\_threshold$  and  $p\_max\_distance$  following the  
 391 process detailed above.

392 Finally, we present the runtimes of the individual modules of Figure 2 in Table 2. These runtimes  
 393 correspond to the 29 runs of the sensitivity analysis. The mean time it takes to run the entire pipeline  
 394 once is 785.68 seconds with a standard deviation of 3.85 seconds. However, results of earlier modules  
 395 can be saved and reused for subsequent module such that for each module previous modules do not have  
 396 to be run again. For the hyperparameter tuning of the parameters in the modules Pipes endpoints and

**Table 2.** Runtime statistics in seconds from applying the pipeline 29 times with different hyperparameters to hydraulic system 1.

Process	n	Median	Mean	Std. deviation	Minimum	Maximum
Preprocessing	29	67.02	67.10	0.52	66.16	68.61
None-pipes object detection	29	3.06	3.09	0.11	3.01	3.60
None-pipes location approximation	29	90.34	90.25	1.55	86.93	92.51
None-pipes matching	29	15.49	15.52	0.14	15.33	15.90
Pipes object detection	29	16.17	16.18	0.13	15.93	16.54
Pipes cleanup	29	14.56	14.54	0.20	14.04	14.84
Pipes matching preprocess	29	553.24	552.02	3.58	544.70	557.84
Pipes matching	29	14.36	14.55	0.79	13.68	16.74
Pipes endpoints	29	1.14	1.05	0.27	0.42	1.48
Graph generation	29	0.58	0.58	0.09	0.41	0.99
Total	29	759.20	758.68	3.85	751.64	766.27

397 Graph generation this means that previous modules do not have to rerun again and various hyperparameter  
398 combinations for  $p\_threshold$ ,  $p\_max\_distance$  and  $graph\_max\_distance$  can be tested as they only take  
399 1.63 seconds on average to evaluate. This enables rapid experimentation and makes the process of setting  
400 the hyperparameters as described above feasible and practical. Experiments were run in parallel on an Intel  
401 Xeon Platinum 8260 CPU and 192 GB RAM.

## 6 DISCUSSION

402 The results presented in Section 4 show that a combination of data acquisition via photogrammetry, object  
403 detection on images and graph generation with an user-defined set of rules is able to generate graphs that are  
404 close to the ground truth for two hydraulic systems. While the detection and matching of relevant objects  
405 and the prediction of their relations and connections works well, the following points should be noted.  
406 Firstly, pipe elbows and T-fittings are treated identical and for both exactly two endpoints are computed,  
407 although T-fittings have three connection points in reality. Rule 2, described as part of the graph generation  
408 process in Section 3.2.3, limits the number of connections of each pipe to a maximum of three. This enables  
409 the method to identify the T-fittings although they are not detected as such initially. Secondly, the location  
410 approximation of non-pipe objects as described in Section 3.2.1 uses some crude heuristics to prevent  
411 the need of time-consuming labelling required for instance segmentation of the objects. Albeit that the  
412 heuristics are crude, they are able to approximate the location of the non-pipe objects sufficiently as shown  
413 in Figure 12. The pumps are the most complex objects and are clearly identifiable in both images. Only the  
414 tank in Figure 12 (A) is hard to identify. However, this is because the side of the tank towards the x-axis is  
415 not included in any of the images and thus cannot be detected. Thirdly, we use a simple approximation  
416 for the pipe endpoints as presented in Section 3.2.2. The results show however that this approximation  
417 is sufficient for connecting most pipe elements. Only the approximation of many small pipe elements in  
418 close proximity as, for example, around the valve between the pumps and tanks in system 2 is challenging.  
419 For the use in digital twins and simulations, it is likely that the individual pipe elements between two  
420 non-pipe objects will be contracted into a single pipe object as it is the case for the graphs in Figure 11 and  
421 12. Hence, the pipe objects between two non-pipe objects are more relevant than how they are connected.  
422 While this means that the pipe predicted by our method will be correctly represented in the simulation  
423 model, it would be preferable to have a more accurate way of approximating endpoints for smaller pipes

424 that will make the prediction of connections more robust. Section 3.2.2 showed that the approximation  
425 performs poorly on pipe elements that are of ambiguous shape, i.e., they are not identifiable as straight or  
426 bent pipe elements. A more precise approximation could alleviate this issue. Fourthly, Section 4 showed  
427 that some subsequent pipe elements were mistakenly matched together resulting in fewer pipe objects  
428 than actually exist. Although technically incorrect, this makes no difference for the functioning of the  
429 digital twin if we apply the same logic as for the previous point assuming that the matched pipe elements  
430 are actually connected in reality. Consider the case where two subsequent pipe elements are detected as  
431 two distinct objects, and the case where the same two pipe elements are falsely matched into a single  
432 object by the pipeline. When the 3D locations of the pipes that are stored in the graph are transferred  
433 into three-dimensional representation, the model will be the same. The only difference is that for the first  
434 case the pipes are connected when transferring the objects into the 3D representation while for the second  
435 case the pipes are already connected before the transfer. The model on which the downstream simulations  
436 are based will be identical and so should the simulation accuracy. Lastly, we want to point out that the  
437 performance of the proposed pipeline of this article is heavily influenced by the quality of the images  
438 and the models used for object detection and instance segmentation. Low-resolution images might not be  
439 accurate enough to accurately predict all relevant objects and segmentation masks might be ambiguous  
440 resulting in the inclusion of other objects or portions of the background. It can also make training more  
441 challenging for the model and prevent it from learning the most important features. Errors made by the  
442 prediction model, e.g., due to shortcomings in the model itself or poor image quality, are challenging to  
443 be reversed downstream in the pipeline. While the multiple perspectives of the images provide multiple  
444 opportunities to detect each object, some objects, such as the sprinklers or the thin vertical pipe in system  
445 2, were not detected by the fine-tuned YOLOv8 model (Redmon et al., 2016) and thus were not included in  
446 the final graphs. To mitigate this issue, (a) the detection model could be improved with more training data  
447 focusing on areas with poor performance, (b) a different model could be explored, or (c) more images of  
448 the hydraulic system could be included that show the challenging objects more clearly.

449 Considering the limitations of the approach presented in this article, future work should address the  
450 approximation of the location of the non-pipe objects and of the pipe endpoints. One possible solution  
451 could be the skeletonization of the pipe elements as discussed in Alex and Stoppe (2025) and Meyer et al.  
452 (2023). Furthermore, although the object detection achieved good results overall, there were issues in  
453 detecting smaller objects, such as sprinklers and thin pipes. It could be investigated if this can be improved  
454 by collecting more images where small objects are depicted prominently, increasing image resolution,  
455 or improving the model, e.g., by exploring the use of vision transformers (Yuan et al., 2021). Updating  
456 the model would not affect the pipeline in any way: The detection models are inputs to the pipeline and  
457 can be replaced with any preferred model. While the differentiation between straight pipes, elbows and  
458 T-fittings worked well in the example test environments, adding them as different object classes in the  
459 'Object detection and instance prediction' module could make the results more robust as it would make  
460 the use of crude heuristics redundant. The models could also be extended to detect more objects than pipes,  
461 pumps, tanks, and valves. This would pave the way for applying the pipeline to environments other than  
462 hydraulic systems. The latter would at the same time help to validate the method further. While the pipeline  
463 shows promising results on generated scenes that mimic real infrastructure, it remains a prototype until  
464 it can be validated on a real-world example. Thus, the main objective for the future remains testing and  
465 validating the pipeline on an actual critical infrastructure.

## 7 CONCLUSION

466 This article proposes a prototypical graph generation pipeline that shows the relations between relevant  
467 predetermined objects that are instrumental to the type of critical infrastructure in question. For example,  
468 this study investigates hydraulic systems for which pipes, reducers, expanders, tanks, valves and pumps  
469 were identified as relevant. The pipeline is based on a combination of photogrammetry, deep learning for  
470 object detection and instance segmentation, and heuristics for inferring relations between objects. The  
471 use of these methods has the advantages of being cost-efficient (both hardware for data collection and  
472 computation) and accessible. The user-defined set of rules for the 'Graph generation' module makes it easy  
473 to tailor the pipeline to specific use cases and transfer it from one problem to the next, while its transparency  
474 and explainability are vital for the high stakes decision-making required for critical infrastructure.

## CONFLICT OF INTEREST STATEMENT

475 The authors declare that the research was conducted in the absence of any commercial or financial  
476 relationships that could be construed as a potential conflict of interest.

## AUTHOR CONTRIBUTIONS

477 MD: Conceptualization, Formal analysis, Investigation, Methodology, Visualization, Writing – original  
478 draft, Writing – review & editing; YT: Conceptualization, Data curation, Formal analysis, Writing –  
479 original draft, Writing – review & editing.

## FUNDING

480 This research was funded by the project Automated Model Generation (AMG) within the German Aerospace  
481 Center (DLR).

## ACKNOWLEDGMENTS

482 We would like to thank our colleagues Sebastian Sporrer, Lena Schreiber and Norman Wilhelms for  
483 their generous assistance, the valuable discussions and their helpful feedback. We further would like  
484 to extend our gratitude to our colleagues Marius Stürmer and Kai Franke for the conceptualization and  
485 implementation of the test environments in the Unreal Engine. This research would not have been possible  
486 without their meticulous work.

## REFERENCES

- 487 Alcaraz, C. and Zeadally, S. (2015). Critical infrastructure protection: Requirements and challenges for the  
488 21st century. *International Journal of Critical Infrastructure Protection* 8, 53–66. doi:10.1016/j.ijcip.  
489 2014.12.002
- 490 Alex, A. and Stoppe, J. (2025). Pipe reconstruction from point cloud data. In *Proceedings of the European*  
491 *Workshop on Maritime Systems Resilience and Security (MARESEC)* (University of Rostock), 1–6.  
492 doi:10.5281/zenodo.17120162
- 493 Borkowski, A. S. (2023). Evolution of BIM: Epistemology, genesis and division into periods. *Journal of*  
494 *Information Technology in Construction* 28. doi:10.36680/j.itcon.2023.034

- 495 Borrmann, A., König, M., Koch, C., and Beetz, J. (2018). Building information modeling: Why? What?  
496 How? In *Building Information Modeling: Technology Foundations and Industry Practice* (Springer).  
497 1–24. doi:10.1007/978-3-319-92862-3\_1
- 498 Buhrmester, V., Münch, D., and Arens, M. (2021). Analysis of explainers of black box deep neural  
499 networks for computer vision: A survey. *Machine Learning and Knowledge Extraction* 3, 966–989.  
500 doi:10.3390/make3040048
- 501 Cheng, L., Wei, Z., Sun, M., Xin, S., Sharf, A., Li, Y., et al. (2020). DeepPipes: Learning 3D pipelines  
502 reconstruction from point clouds. *Graphical Models* 111, 101079. doi:10.1016/j.gmod.2020.101079
- 503 Codex Labs (2022). *Colosseum: A high-fidelity simulator for autonomous vehicles (Fork of AirSim)*. Codex  
504 Labs LLC. Version 2.1.0. Available at <https://github.com/CodexLabsLLC/Colosseum>.  
505 Accessed: 2025-11-13
- 506 Cong, Y., Yang, M. Y., and Rosenhahn, B. (2023). RelTR: Relation transformer for scene graph generation.  
507 *IEEE Transactions on Pattern Analysis and Machine Intelligence* 45, 11169–11183. doi:10.1109/TPAMI.  
508 2023.3268066
- 509 Dosovitskiy, A., Beyer, L., Kolesnikov, A., Weissenborn, D., Zhai, X., Unterthiner, T., et al. (2021). An  
510 image is worth 16x16 words: Transformers for image recognition at scale. In *International Conference*  
511 *on Learning Representations (ICLR)*. 1–22
- 512 Dwivedi, R., Dave, D., Naik, H., Singhal, S., Omer, R., Patel, P., et al. (2023). Explainable AI (XAI): Core  
513 ideas, techniques, and solutions. *ACM Computing Surveys* 55, 1–33. doi:10.1145/3561048
- 514 Epic Games (2022a). *Lumen Global Illumination and Reflections*. Epic Games, Inc. Available  
515 at [https://dev.epicgames.com/documentation/en-us/unreal-engine/  
516 lumen-global-illumination-and-reflections-in-unreal-engine](https://dev.epicgames.com/documentation/en-us/unreal-engine/lumen-global-illumination-and-reflections-in-unreal-engine). Accessed:  
517 2026-01-23
- 518 Epic Games (2022b). *Nanite Virtualized Geometry*. Epic Games, Inc. Available  
519 at [https://dev.epicgames.com/documentation/en-us/unreal-engine/  
520 nanite-in-unreal-engine](https://dev.epicgames.com/documentation/en-us/unreal-engine/nanite-in-unreal-engine). Accessed: 2026-01-23
- 521 Epic Games (2022c). *Unreal Engine 5*. Epic Games, Inc. Version 5.1. Available at [https://www.  
522 unrealengine.com/](https://www.unrealengine.com/). Accessed: 2025-11-13
- 523 Ester, M., Kriegel, H.-P., Sander, J., Xu, X., et al. (1996). A density-based algorithm for discovering clusters  
524 in large spatial databases with noise. In *Proceedings of the International Conference on Knowledge*  
525 *Discovery and Data Mining (KDD)* (ACM), 226–231
- 526 Franke, K., Stürmer, J. M., and Koch, T. (2023). Automated simulation and virtual reality coupling for  
527 interactive digital twins. In *Proceedings of the Winter Simulation Conference (WSC)* (IEEE), 2615–2626.  
528 doi:10.1109/WSC60868.2023.10407185
- 529 Gao, X., Xiao, B., Tao, D., and Li, X. (2010). A survey of graph edit distance. *Pattern Analysis and*  
530 *applications* 13, 113–129
- 531 Ghaffarianhoseini, A., Tookey, J., Ghaffarianhoseini, A., Naismith, N., Azhar, S., Efimova, O., et al. (2017).  
532 Building information modelling (BIM) uptake: Clear benefits, understanding its implementation, risks  
533 and challenges. *Renewable and Sustainable Energy Reviews* 75, 1046–1053. doi:10.1016/j.rser.2016.11.  
534 083
- 535 Goesele, M., Curless, B., and Seitz, S. (2006). Multi-View Stereo revisited. In *Proceedings of the*  
536 *Conference on Computer Vision and Pattern Recognition (CVPR)* (IEEE/CVF), vol. 2, 2402–2409.  
537 doi:10.1109/CVPR.2006.199
- 538 Grieves, M. (2014). Digital twin: Manufacturing excellence through virtual factory replication. *Whitepaper*  
539 1, 1–7

- 540 Hart, L., Knoblach, S., and Möser, M. (2023). Automated pipeline reconstruction using deep learning  
541 & instance segmentation. *ISPRS Open Journal of Photogrammetry and Remote Sensing* 9, 100043.  
542 doi:10.1016/j.ojphoto.2023.100043
- 543 Hartley, R. and Zisserman, A. (2003). *Multiple View Geometry in Computer Vision* (Cambridge: Cambridge  
544 University Press), 2nd edn.
- 545 He, K., Gkioxari, G., Dollár, P., and Girshick, R. (2017). Mask R-CNN. In *Proceedings of the International  
546 Conference on Computer Vision (ICCV)* (IEEE/CVF), 2961–2969. doi:10.1109/ICCV.2017.322
- 547 Jones, D., Snider, C., Nassehi, A., Yon, J., and Hicks, B. (2020). Characterising the digital twin: A  
548 systematic literature review. *CIRP Journal of Manufacturing Science and Technology* 29, 36–52.  
549 doi:10.1016/j.cirpj.2020.02.002
- 550 Kawashima, K., Kanai, S., and Date, H. (2014). As-built modeling of piping system from terrestrial  
551 laser-scanned point clouds using normal-based region growing. *Journal of Computational Design and  
552 Engineering* 1, 13–26. doi:10.7315/JCDE.2014.002
- 553 Kirillov, A., Mintun, E., Ravi, N., Mao, H., Rolland, C., Gustafson, L., et al. (2023). Segment anything.  
554 In *Proceedings of the International Conference on Computer Vision (ICCV)* (IEEE/CVF), 4015–4026.  
555 doi:10.1109/ICCV51070.2023.00371
- 556 Lampropoulos, G., Larrucea, X., and Colomo-Palacios, R. (2024). Digital twins in critical infrastructure.  
557 *Information* 15, 454. doi:10.3390/info15080454
- 558 Li, H., Zhu, G., Zhang, L., Jiang, Y., Dang, Y., Hou, H., et al. (2024). Scene graph generation: A  
559 comprehensive survey. *Neurocomputing* 566, 127052. doi:10.1016/j.neucom.2023.127052
- 560 Lin, T.-Y., Maire, M., Belongie, S., Hays, J., Perona, P., Ramanan, D., et al. (2014). Microsoft COCO:  
561 Common objects in context. In *Proceedings of the European Conference on Computer Vision (ECCV)*  
562 (Springer), 740–755. doi:10.1007/978-3-319-10602-1\_48
- 563 Lu, Q., Xie, X., Parlikad, A. K., Schooling, J. M., and Konstantinou, E. (2022). Moving from building  
564 information models to digital twins for operation and maintenance. *Proceedings of the Institution of  
565 Civil Engineers-Smart Infrastructure and Construction* 174, 46–56. doi:10.1680/jsmic.19.00011
- 566 Lv, C., Qi, M., Li, X., Yang, Z., and Ma, H. (2024). SGFormer: Semantic graph transformer for point  
567 cloud-based 3D scene graph generation. In *Proceedings of the AAAI Conference on Artificial Intelligence*  
568 (AAAI), vol. 38, 4035–4043. doi:10.1609/aaai.v38i5.28197
- 569 Meyer, L., Gilson, A., Scholz, O., and Stamminger, M. (2023). CherryPicker: Semantic skeletonization and  
570 topological reconstruction of cherry trees. In *Conference on Computer Vision and Pattern Recognition  
571 Workshops (CVPRW)* (IEEE/CVF), 6244–6253. doi:10.1109/CVPRW59228.2023.00664
- 572 Moon, D., Chung, S., Kwon, S., Seo, J., and Shin, J. (2019). Comparison and utilization of point  
573 cloud generated from photogrammetry and laser scanning: 3D world model for smart heavy equipment  
574 planning. *Automation in Construction* 98, 322–331. doi:10.1016/j.autcon.2018.07.020
- 575 Osei-Kyei, R., Tam, V., Ma, M., and Mashiri, F. (2021). Critical review of the threats affecting the  
576 building of critical infrastructure resilience. *International Journal of Disaster Risk Reduction* 60, 102316.  
577 doi:10.1016/j.ijdrr.2021.102316
- 578 Peng, J., Liu, Q., Yue, L., Zhang, Z., Zhang, K., and Sha, Y. (2024). Towards few-shot self-explaining graph  
579 neural networks. In *Proceedings of the Joint European Conference on Machine Learning and Knowledge  
580 Discovery in Databases (ECML PKDD)* (Springer), 109–126. doi:10.1007/978-3-031-70365-2\_7
- 581 Qiu, R., Zhou, Q.-Y., and Neumann, U. (2014). Pipe-run extraction and reconstruction from point  
582 clouds. In *Proceedings of the European Conference on Computer Vision (ECCV)* (Springer), 17–30.  
583 doi:10.1007/978-3-319-10578-9\_2

- 584 Redmon, J., Divvala, S., Girshick, R., and Farhadi, A. (2016). You only look once: Unified, real-time  
585 object detection. In *Proceedings of the Conference on Computer Vision and Pattern Recognition (CVPR)*  
586 (IEEE/CVF), 779–788. doi:10.1109/CVPR.2016.91
- 587 Rudin, C. (2019). Stop explaining black box machine learning models for high stakes decisions and use  
588 interpretable models instead. *Nature Machine Intelligence* 1, 206–215. doi:10.1038/s42256-019-0048-x
- 589 Şahin, E., Arslan, N. N., and Özdemir, D. (2025). Unlocking the black box: An in-depth review on  
590 interpretability, explainability, and reliability in deep learning. *Neural Computing and Applications* 37,  
591 859–965. doi:10.1007/s00521-024-10437-2
- 592 Schönberger, J. L. and Frahm, J.-M. (2016). Structure-from-Motion revisited. In *Proceedings of the*  
593 *Conference on Computer Vision and Pattern Recognition (CVPR)* (IEEE/CVF), 4104–4113. doi:10.  
594 1109/CVPR.2016.445
- 595 Schreiber, L. R., Tarant, Y. E., and Franke, K. (2024). Synthetic training data bias in instance segmentation  
596 algorithms. In *Artificial Intelligence for Security and Defence Applications II* (SPIE), vol. 13206,  
597 198–208. doi:10.1117/12.3030822
- 598 Schubert, E., Sander, J., Ester, M., Kriegel, H. P., and Xu, X. (2017). DBSCAN revisited, revisited: Why  
599 and how you should (still) use DBSCAN. *ACM Transactions on Database Systems (TODS)* 42, 1–21.  
600 doi:10.1145/3068335
- 601 Shah, S., Dey, D., Lovett, C., and Kapoor, A. (2017). AirSim: High-fidelity visual and physical simulation  
602 for autonomous vehicles. In *Proceedings of the Field and Service Robotics (FSR)* (Springer), 621–635.  
603 doi:10.1007/978-3-319-67361-5\_40
- 604 Shit, S., Koner, R., Wittmann, B., Paetzold, J., Ezhov, I., Li, H., et al. (2022). Relationformer: A unified  
605 framework for image-to-graph generation. In *Proceedings of the European Conference on Computer*  
606 *Vision (ECCV)* (Springer), 422–439. doi:10.1007/978-3-031-19836-6\_24
- 607 Sousa, B., Arieiro, M., Pereira, V., Correia, J., Lourenço, N., and Cruz, T. (2021). ELEGANT: Security of  
608 critical infrastructures with digital twins. *IEEE Access* 9, 107574–107588. doi:10.1109/ACCESS.2021.  
609 3100708
- 610 Vidas, S., Moghadam, P., and Bosse, M. (2013). 3D thermal mapping of building interiors using an RGB-D  
611 and thermal camera. In *Proceedings of the International Conference on Robotics and Automation (ICRA)*  
612 (IEEE), 2311–2318. doi:10.1109/ICRA.2013.6630890
- 613 Wald, J., Avetisyan, A., Navab, N., Tombari, F., and Nießner, M. (2019). Rio: 3D object instance  
614 re-localization in changing indoor environments. In *Proceedings of the International Conference on*  
615 *Computer Vision (ICCV)* (IEEE/CVF), 7658–7667. doi:10.1109/ICCV.2019.00775
- 616 Wald, J., Dharmo, H., Navab, N., and Tombari, F. (2020). Learning 3D semantic scene graphs from 3D  
617 indoor reconstructions. In *Proceedings of the Conference on Computer Vision and Pattern Recognition*  
618 *(CVPR)* (IEEE/CVF), 3961–3970. doi:10.1109/CVPR42600.2020.00402
- 619 Xu, F., Uszkoreit, H., Du, Y., Fan, W., Zhao, D., and Zhu, J. (2019). Explainable AI: A brief survey  
620 on history, research areas, approaches and challenges. In *Proceedings of the CFF International*  
621 *Conference on Natural Language Processing and Chinese Computing (NLPCC)* (Springer), 563–574.  
622 doi:10.1007/978-3-030-32236-6\_51
- 623 Yang, J., Lu, J., Lee, S., Batra, D., and Parikh, D. (2018). Graph R-CNN for scene graph generation. In  
624 *Proceedings of the European Conference on Computer Vision (ECCV)* (Springer), 670–685. doi:10.  
625 1007/978-3-030-01246-5\_41
- 626 Yeo, Q. X., Li, Y., and Lee, G. H. (2025). Statistical confidence rescoring for robust 3D scene graph  
627 generation from multi-view images. In *Proceedings of the International Conference on Computer Vision*  
628 *(ICCV)* (IEEE/CVF), 24999–25008

- 629 Yuan, L., Chen, Y., Wang, T., Yu, W., Shi, Y., Jiang, Z.-H., et al. (2021). Tokens-to-token ViT: Training  
630 vision transformers from scratch on ImageNet. In *Proceedings of the International Conference on*  
631 *Computer Vision (ICCV)* (IEEE/CVF), 558–567. doi:10.1109/ICCV48922.2021.00060
- 632 Yusta, J. M., Correa, G. J., and Lacal-Arántegui, R. (2011). Methodologies and applications for critical  
633 infrastructure protection: State-of-the-art. *Energy Policy* 39, 6100–6119. doi:10.1016/j.enpol.2011.07.  
634 010
- 635 Zhang, Z., Liu, Q., Wang, H., Lu, C., and Lee, C. (2022). ProtGNN: Towards self-explaining graph neural  
636 networks. In *Proceedings of the Conference on Artificial Intelligence (AAAI)*, vol. 36, 9127–9135.  
637 doi:10.1609/aaai.v36i8.20898
- 638 Zhao, H., Xia, R., Chen, Y., Zhang, T., Fu, D., and Zhang, T. (2025). A multi-camera vision online  
639 measurement method for complex tube parameters based on regional pre-segmentation. *Journal of*  
640 *Manufacturing Processes* 149, 502–517. doi:10.1016/j.jmapro.2025.05.083
- 641 Zhou, Y. and Tuzel, O. (2018). VoxelNet: End-to-end learning for point cloud based 3D object detection.  
642 In *Proceedings of the Conference on Computer Vision and Pattern Recognition (CVPR)* (IEEE/CVF),  
643 4490–4499. doi:10.1109/CVPR.2018.00472
- 644 Zimmer, W., Ercelik, E., Zhou, X., Ortiz, X. J. D., and Knoll, A. (2022). A survey of robust 3D object  
645 detection methods in point clouds. *arXiv:2204.00106 [Preprint]*. Available at [https://doi.org/](https://doi.org/10.48550/arXiv.2204.00106)  
646 [10.48550/arXiv.2204.00106](https://doi.org/10.48550/arXiv.2204.00106) (Accessed November 13, 2025)